



OPEN

Evidence of shock-compressed stishovite above 300 GPa

Markus O. Schoelmerich¹✉, Thomas Tschentscher¹, Shrikant Bhat², Cindy A. Bolme³, Eric Cunningham⁴, Robert Farla², Eric Galtier⁴, Arianna E. Gleason⁴, Marion Harmand⁵, Yuichi Inubushi^{6,7}, Kento Katagiri⁸, Kohei Miyanishi⁶, Bob Nagler⁴, Norimasa Ozaki⁸, Thomas R. Preston¹, Ronald Redmer⁹, Ray F. Smith¹⁰, Tsubasa Tobase¹¹, Tadashi Togashi^{6,7}, Sally J. Tracy¹², Yuhei Umeda⁸, Lennart Wollenweber¹, Toshinori Yabuuchi^{6,7}, Ulf Zastrau¹ & Karen Appel¹

SiO₂ is one of the most fundamental constituents in planetary bodies, being an essential building block of major mineral phases in the crust and mantle of terrestrial planets (1–10 M_E). Silica at depths greater than 300 km may be present in the form of the rutile-type, high pressure polymorph stishovite (*P4₂/mnm*) and its thermodynamic stability is of great interest for understanding the seismic and dynamic structure of planetary interiors. Previous studies on stishovite via static and dynamic (shock) compression techniques are contradictory and the observed differences in the lattice-level response is still not clearly understood. Here, laser-induced shock compression experiments at the LCLS- and SACLA XFEL light-sources elucidate the high-pressure behavior of stishovite on the lattice-level under *in situ* conditions on the Hugoniot to pressures above 300 GPa. We find stishovite is still (meta-)stable at these conditions, and does not undergo any phase transitions. This contradicts static experiments showing structural transformations to the CaCl₂, α-PbO₂ and pyrite-type structures. However, rate-limited kinetic hindrance may explain our observations. These results are important to our understanding into the validity of EOS data from nanosecond experiments for geophysical applications.

Stishovite, the high-pressure polymorph of silica, is of vast interest for planetary- and material science as a dominant constituent material in the mantle of Earth and larger terrestrial extra-solar planets. Under equilibrium conditions, stishovite becomes the stable form of SiO₂ at pressures above ~7 GPa and crystallizes in the rutile-type structure (*P4₂/mnm*), consisting of octahedrally coordinated Si atoms^{1–3}. Static compression studies using diamond anvil cell (DAC) techniques show, that stishovite undergoes a displacive phase transition to the orthorhombic CaCl₂-type structure (*Pnmm*) at ~60 GPa^{4–10} and a further transition to the α-PbO₂ type structure (*Pbcn*) at ~121 GPa^{10–16}. To date, the highest-pressure experimentally determined SiO₂ phase transformation is to the pyrite-type structure (*Pa* $\bar{3}$) at around 268 GPa¹⁷.

Additionally, silica has been explored using dynamic shock compression experiments. Shock compression studies of fused silica and quartz up to 200 GPa indicate phase transitions to stishovite, post-stishovite phase(s) and melting above 120 GPa^{18–23}. However, only few studies use stishovite as a starting material. This is mainly due to the difficulty of synthesizing large specimens of stishovite without impurities or significant porosity, and preparing these samples for shock compression experiments. Stishovite has been shock compressed in the pressure regime between 193.6–235.7 GPa with the gas gun technique²⁴, between 316–992 GPa with the flyer plate technique at the Z-machine²⁵ and in the pressure regime between 1032.2–2660.4 GPa with the decaying shock method at the OMEGA laser facility²⁶. All three studies resolve the stishovite continuum Hugoniot. In contrast to static experiments⁵, there is no indication of a phase transition to post-stishovite structures. This was previously

¹European XFEL, Schenefeld, 22869, Germany. ²Photon Science, Deutsches Elektronen-Synchrotron DESY, Hamburg, 22607, Germany. ³Los Alamos National Laboratory, Los Alamos, New Mexico, 87545, USA. ⁴SLAC National Accelerator Laboratory, Menlo Park, CA, 94025, USA. ⁵Institute of Mineralogy, Materials Physics and Cosmochemistry, Sorbonne Universités, Paris, 75005, France. ⁶RIKEN SPring-8 Center, Sayo-cho, Sayo-gun, Hyogo, 679-5148, Japan. ⁷Japan Synchrotron Radiation Research Institute, Sayo-cho, Sayo-gun, Hyogo, 679-5198, Japan. ⁸Osaka University, Suita, Osaka, 565-0871, Japan. ⁹Universität Rostock, Institut für Physik, Rostock, 18051, Germany. ¹⁰Lawrence Livermore National Laboratory, Livermore, CA, 94500, USA. ¹¹Center for High-Pressure Science and Technology Advanced Research (HPSTAR), Shanghai, 201203, China. ¹²Earth and Planets Laboratory, Carnegie Institution of Washington, Washington, D.C., 20015, USA. ✉e-mail: markus.schoelmerich@xfel.eu

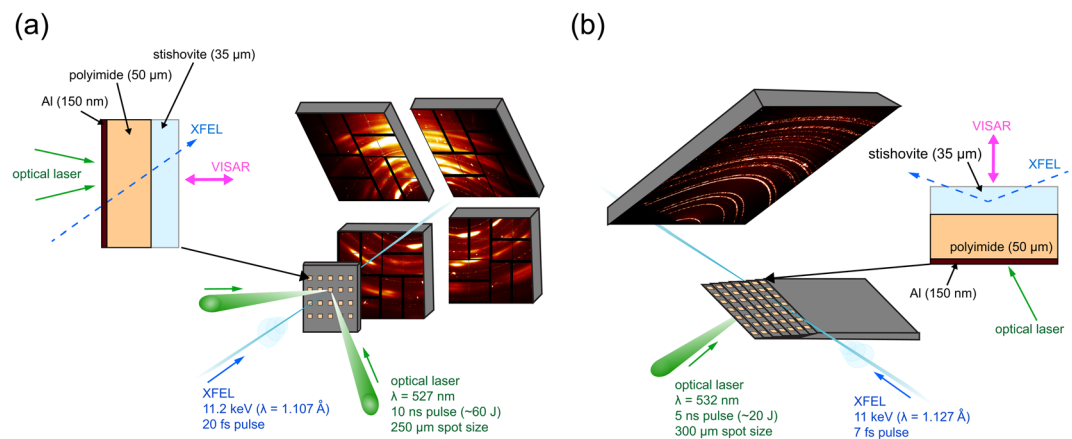


Figure 1. (a) Experimental setup arranged in transmission Debye-Scherrer geometry at the MEC end station of the LCLS. Dual drive laser beams were incident on samples at 15° and the XFEL beam at 30° from the target normal. (b) Experimental setup in Bragg geometry at the BL3:EH5 of SACLA. Grazing-incidence angle of the XFEL towards the target was 18° and drive laser beam was incident on samples at 18° from the target normal.

Run	U_p (km/s)	U_s (km/s)	P_{VISAR} (GPa)	$E-E_0$ (kJ/mol)	V (Å ³)	ρ (g/cm ³)	a (Å)	c (Å)
SACLA-795997	n.a.	n.a.	ambient	n.a.	46.5 (2)	4.30 (2)	4.176 (8)	2.664 (6)
SACLA-796485	0.45 (2)	9.66 (53)	18 (2)	0.10 (1)	44.3 (3)	4.51 (5)	4.09 (1)	2.65 (1)
SACLA-796491	2.38 (4)	12.10 (25)	123 (5)	2.82 (12)	37.3 (2)	5.35 (4)	3.85 (1)	2.513 (9)
LCLS-235	4.75 (8)	14.76 (31)	301 (12)	11.28 (48)	31.8 (4)	6.3 (1)	3.69 (2)	2.33 (2)
LCLS-233*	4.90 (8)	15.04 (45)	317 (15)	12.01 (56)	31.3 (9)	6.4 (3)	n.a.	n.a.
LCLS-239	5.10 (9)	15.35 (31)	336 (13)	13.01 (51)	31.0 (4)	6.44 (8)	3.66 (2)	2.32 (1)

Table 1. Experimental results from this study. Particle and shock velocities U_p and U_s , as well as pressures and energies were determined with the VISAR (see Supplementary Material). Volume, density and lattice parameter a and c were obtained from refined XRD spectra. *No XRD information is available for run233. All results from run233 were solely determined through velocimetry data.

explained by either sluggish kinetics as a result of the low compressibility of stishovite or the relatively small volume changes accompanying post-stishovite phase transitions, which cannot be readily distinguished from the stishovite Hugoniot²⁴.

Until now, the highest pressures for which *in-situ* structural information of stishovite was obtained are from static compression experiments with a diamond anvil cell at 128 GPa⁵ and there are no structural observations from any shock-compression experiments. The high initial density and low compressibility allowed us to shock-compress stishovite in the solid phase to pressures above 300 GPa. The concurrent use of the brilliant and coherent X-rays at the Linac Coherent Light Source (LCLS) and SPring-8 Angstrom Compact free electron Laser (SACLA), enabled the determination of the structural response under shock loading on the lattice-level of stishovite at these conditions for the first time.

Results

The experiments were carried out at the Matter at Extreme Conditions (MEC) end station of the LCLS- and the BL3:EH5 end station of the SACLA X-ray Free Electron Laser (XFEL). The experimental setups are shown in Fig. 1. Polycrystalline stishovite was synthesized in a large volume press at the P61B end station of PETRA III at the German Electron-Synchrotron (DESY) with an initial density of $\rho_0 = 4.30 \text{ g/cm}^3$ (Table 1, run795997). Stishovite samples were cut and polished to 35 μm. Targets were subsequently glued to 50 μm polyimide (kapton) tape and shock compressed using optical drive lasers. Derived from hydrodynamic simulations, steady uniform pressure conditions within the sample are achieved within a time span of ~1–5 ns for the high pressure drives (see Supplementary Material). The samples were probed with an 11.2 keV (LCLS) and 11 keV (SACLA) XFEL X-ray pulse when the majority of it was in the compressed state. This was determined from the shock breakout via the velocity interferometer system for any reflector (VISAR). The VISAR measured the rear free surface velocity of stishovite for each shot from which particle velocity (U_p), shock wave velocity (U_s) and pressure in the shocked state were determined (see Supplementary Material).

The shock and particle velocities (Table 1) obtained in this study yield a linear fit in the high pressure regime

$$U_s(\text{km/s}) = 1.21 U_p + 9.155 \quad (1)$$

and are in excellent agreement with literature data²⁴. Pressures P and internal energies E were calculated using the Rankine-Hugoniot equations:

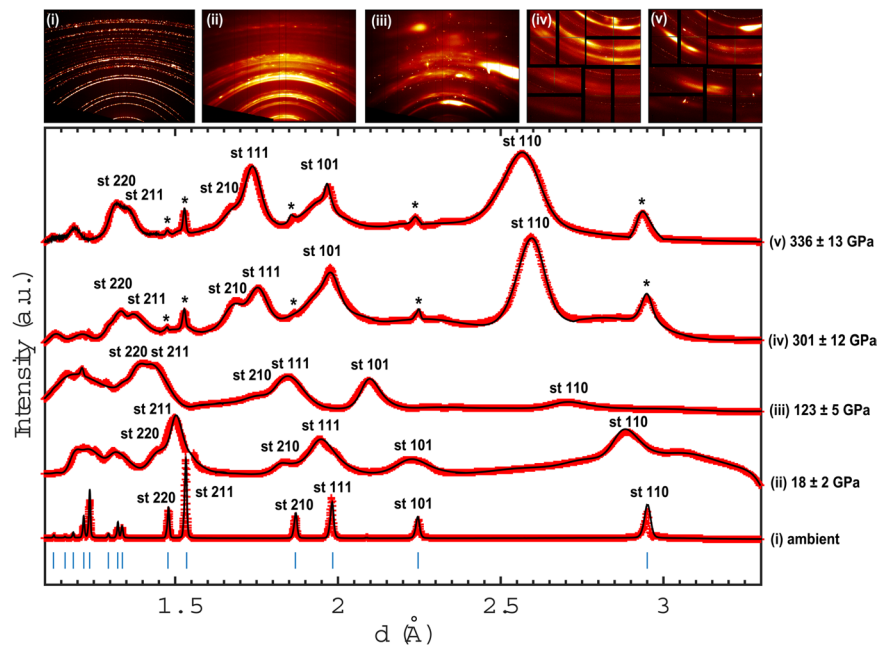


Figure 2. Multiplot of XRD pattern of stishovite. Observed d-spacing (red crosses) and Le Bail-fitted pattern (black line) of stishovite at ambient conditions, 18 ± 2 GPa, 123 ± 5 GPa, 301 ± 12 GPa and 336 ± 13 GPa. Stishovite reflections are indexed at each peak. Ambient peaks are indicated with an asterisk. Note that peaks are shifting to lower d-spacing values due to the change in volume of the lattice with increasing pressure.

$$P - P_0 = \rho_0 U_s U_p \quad (2)$$

$$E - E_0 = \frac{1}{2}(P + P_0)(1/\rho_0 - 1/\rho) \quad (3)$$

here, E_0 , P_0 and ρ_0 are reference values at ambient state. Results are listed in Table 1. Pressures obtained from the VISAR agree within 2–6% to EOS data from literature²⁴ and density functional theory (DFT) simulations (see Supplementary Table S2).

Bragg reflections of stishovite are observed upon shock loading up to 336 ± 13 GPa (Fig. 2). The stishovite structure from the refined diffraction pattern at 18 ± 2 GPa reveals a relative change in volume of $V/V_0 = 0.95$ at a density of 4.51 g/cm^3 . The achieved pressure is well within the stishovite stability field found in static compression experiments^{2,5,10,27–30}. However, a departure from equilibrium behavior is observed at higher pressures: at 123 ± 5 GPa, Bragg reflections of compressed stishovite are still apparent and refined lattice parameters reveal a relative volume change of $V/V_0 = 0.80$ at a density of 5.35 g/cm^3 . These conditions are within the equilibrium phase stability field of α - PbO_2 type silica^{10–16}. At higher pressures, Bragg reflections of compressed and ambient (marked with an asterisk) stishovite are observed. The refined stishovite reflections at 301 ± 12 GPa indicate a volume change of $V/V_0 = 0.69$ at a density of 6.3 g/cm^3 . At 317 ± 15 GPa, density and volume was determined through the VISAR and indicates a relative volume change of $V/V_0 = 0.67$ and a shock-density of 6.4 g/cm^3 . At 336 ± 13 GPa, the highest achieved pressure within stishovite in this study, exhibits a volume change of $V/V_0 = 0.66$ at a density of 6.44 g/cm^3 .

The pressures, determined from VISAR, as a function of density, obtained from XRD, are shown in Fig. 3. They are in excellent agreement with literature data from shock compression experiments^{24–26} and below 128 GPa comparable to static compression experiments^{5,27–30}. We estimated the equation of state (EOS) of stishovite by fitting the data with the EosFit software³¹ to the third-order Birch-Murnaghan equation of state³² and, to compare to static data, corrected the shock wave data to a 300 K isotherm. The 300 K isotherm was calculated by subtracting the thermal pressure from the shocked state at fixed volume²⁷. We determined the pressure correction by calculating the temperature along the Hugoniot²⁶ (see Supplementary Material) and the pressure difference between the Hugoniot and 300 K isotherm using the Grüneisen parameter

$$\gamma(V) = \gamma_0 \left(\frac{V}{V_0} \right)^q \quad (4)$$

with given literature values for q ²⁴ and γ_0 ³³. The shock wave data fit yields a bulk modulus of $K_0 = 307 \pm 4$ GPa and its first pressure derivative $K_0' = 4.66 \pm 0.15$ GPa in the range of 0–336 GPa, which is in excellent accordance to literature data of shock compression experiments ($K_0 = 315$ GPa, $K_0' = 4.8$ GPa¹⁸; $K_0 = 307$ GPa, $K_0' = 5.0$ GPa²⁴) as

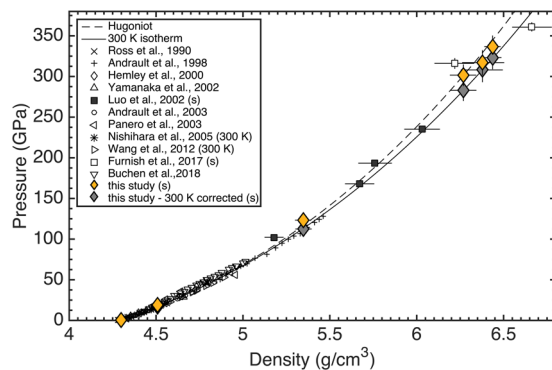


Figure 3. Pressure-density experimental data for stishovite (yellow diamonds) and 300 K corrected data (grey diamonds) from this study and literature. (s) indicates shock wave experiments. Drawn are furthermore the stishovite Hugoniot (dashed line) and 300 K isotherm (solid line).

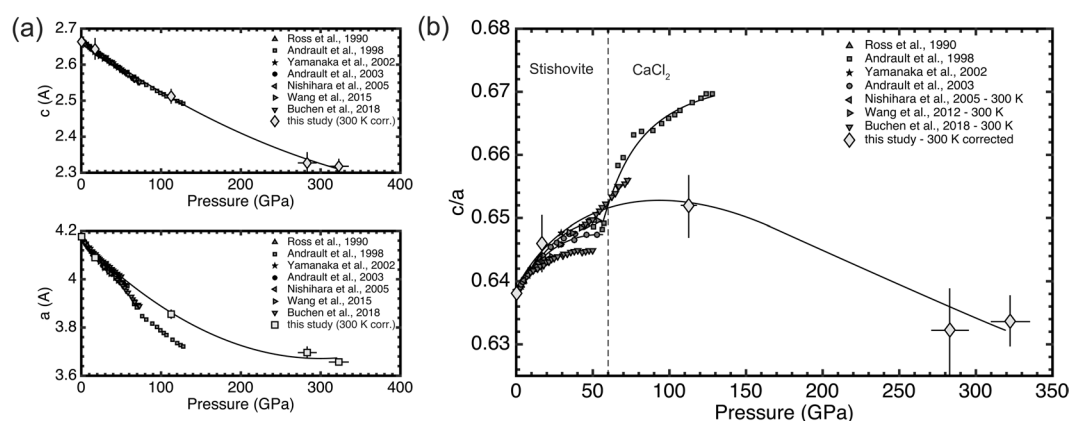


Figure 4. (a) Unit-cell parameters a and c of stishovite with regard to pressure. (b) Lattice parameter ratio c/a with regard to pressure. Indicated is furthermore the pressure, at which a structural transformation from stishovite to CaCl_2 -type silica has been observed in static experiments^{5,34} (dashed line).

well as EOS studies of stishovite at lower pressures from static DAC experiments ($K_0 = 309.9 \text{ GPa}$, $K_0' = 4.59 \text{ GPa}^5$; $K_0 = 294 \text{ GPa}$, $K_0' = 4.85 \text{ GPa}^{27}$).

Pressure evolution of the SiO_2 unit-cell parameters from refined XRD pattern are shown in Fig. 4. Here, a deviation from static data^{5,34} is observed for the lattice parameter a at pressures exceeding $\sim 60 \text{ GPa}$ (Fig. 4a). The lattice parameter ratio c/a rises with increasing pressures from ~ 0.638 at ambient conditions to ~ 0.650 at 123 GPa (Fig. 4b). In this regime the compressibility of the lattice parameter a is higher than for lattice parameter c . However, at $\sim 123 \text{ GPa}$, this trend is reversing and lattice parameter c seems to be more compressible than lattice parameter a with a decreasing lattice parameter ratio c/a from ~ 0.650 at 123 GPa to ~ 0.634 at 336 GPa .

Discussion

The results of this study on shock compressed stishovite observed by *in-situ* X-ray diffraction differ strongly from static compression experiments at respective pressures (Fig. 5). X-ray diffraction studies on stishovite with a DAC show a distinct phase transformation at $\sim 60 \text{ GPa}$ to the CaCl_2 type silica^{5,34}. This is, however, in contrast to previous shock compression experiments, where the displacive transition towards CaCl_2 does not appear in continuum Hugoniot data^{24–26}.

Our experimental data is in good accordance with the stishovite EOS of static and shock experiments^{5,24} (Fig. 3) and the bulk moduli from our experiment agree within 1–4% to literature data^{5,18,24,27}. It seems that this is not only valid at lower pressures, but continues to be apparent at multi-Mbar pressures^{25,26}. Past studies have interpreted the lack of evidence for a phase transition as i) not being in the right pressure regime, ii) sluggish kinetics, or iii) relatively small changes in structure and energy attending a phase transition and not detectable with diagnostics²⁴. Up to now, however, there is no lattice-level structural information for stishovite under shock compression. By coupling XFEL sources to high-power laser systems, we can now reveal subtle changes in lattice structure during the shock response of materials. The femtosecond diffraction contradicts i) and iii), since Bragg reflections of stishovite can still be observed in the shock compressed state along the respective Hugoniot at pressures exceeding 300 GPa . Furthermore, the measured lattice parameters do not indicate a change in crystal structure as in a first order transition, in contrast to static data^{5,34} (Fig. 4). The stishovite structure of our shock compression

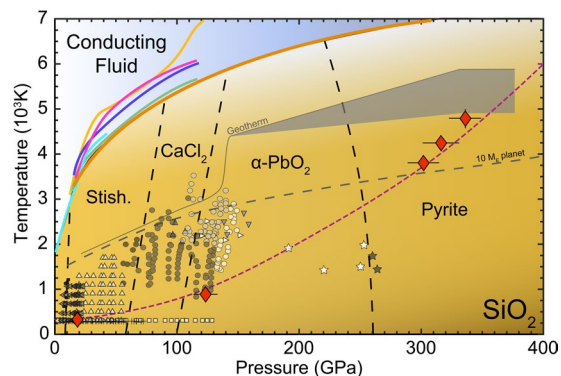


Figure 5. SiO_2 phase diagram, modified after^{18,26,47}. Shown is experimental data where the structure of SiO_2 was resolved. Indicated are the different equilibrium phase stability fields and the geotherms of Earth and terrestrial planets with a mass of $10 M_E$. Red diamonds are data from this study and the dashed magenta line indicates the Sesame stishovite EOS 7360⁵⁰. Shown is data with quartz or fused silica as a starting material: black and grey squares from², circles from¹⁰, right triangles from¹², lower triangles from¹⁵ and stars from¹⁷ as well as stishovite as a starting material: white squares⁴, upper triangles²⁷, crosses³⁴ and left triangles²⁸. Furthermore melting lines are indicated: brown²⁶, orange⁵¹, pink⁵², blue⁵³, green⁵⁴ and light blue^{55,56}.

experiments above 300 GPa is therefore in vast contrast to static compression experiments: at 123 GPa, there is no indication of a $\alpha\text{-PbO}_2$ phase, which was seen in DAC experiments with SiO_2 ^{10,12} and at experimental peak pressures of 301 GPa to 336 GPa there is no indication of the pyrite structure¹⁷ at these timescales.

The differences in relative compression between lattice parameter a and c in our study indicates an anisotropic compression. As predicted by density functional theory, a is initially more compressible than c but the anisotropic behavior of a becomes less pronounced at higher pressure³⁵. The relative lattice parameter compression (Fig. 4) even suggests, that this trend eventually reverses and that the polycrystalline stishovite was preferentially orientated within the c -direction during shock transit. Additionally, the broadening of the Bragg reflections in Fig. 2 indicate a pressure gradient and non-hydrostatic stress, with the accuracy of the measured d -values being diminished. It is well known from static (DAC) experiments and molecular dynamic simulations, that (non-) hydrostaticity can fundamentally change the onset, or presence, of phase transitions^{36,37}. Previous studies on stishovite in static experiments show, that non-hydrostaticity produces large deviatoric stresses as a result of the high shear strength^{7,9} and it was observed, that the preferred orientation of stishovite under compression is the crystallographic c -direction³⁸. However, it was suggested, that non-hydrostatic conditions in DACs actually decrease the pressure-induced onset of a ferroelastic phase transitions from the tetragonal (stishovite) to the orthorhombic (CaCl_2) structure⁸. This might be different for shock compression experiments in which it is argued, that non-hydrostatic stresses may displace the equilibrium boundaries to higher stresses^{39,40}.

In addition to anisotropic compression, due to the absence of phase transformations, shock temperature rises with increasing pressure to adjust to the increase of internal energy due to the compression work²⁶. Our calculations indicate, that stishovite is experiencing temperatures ranging from 324 up to 4757 K over a pressure range of 18 to 336 GPa during shock loading (Fig. 5). However, because of the nanosecond timescales during dynamic loading and accommodation of rate-limiting kinetic hinderances, effects can result in significant shifts of equilibrium phase boundaries such that transitions may not be observed or may require significant overpressure. This is a known deviation between shock and static experiments^{41–46}. However, the extent to which these pressure induced phase transformations can be hindered seems to be much more pronounced for stishovite than for other materials, presumably due to its high initial density and low compressibility. Our results are unexpected as one would not presume crystallization to be inhibited, at least for the CaCl_2 structure, which is differentiated from stishovite only by a small diffusionless displacement of oxygen ions.

The pressure and temperature range encompassed in this study is comparable to Super-Earth ($1\text{--}10 M_E$) interior conditions (Fig. 5). However and contrary to our results, it is well established from experimental observation that a stable stishovite structure within the Earth's mantle at pressures exceeding ~ 60 GPa is improbable⁴⁷. This can be explained by the short timescales (few ns) involved during our shock compression experiments, which can prevent the observation of long time scale phase transitions as in equilibrated planetary interiors. Indeed, certain phase transitions require at least several nanoseconds to be triggered and can only be observed at longer time scales²⁰. Therefore, further time dependence studies under shocked SiO_2 should be foreseen to bring possible constraints on its physical and chemical properties inside Super-Earth interiors.

In summary, we have determined the shock response of stishovite under shock loading via XRD from the LCLS and SACLA XFEL sources. Additional velocimetry diagnostics confirmed shock data from literature, and provided evidence of the departure from equilibrium behavior of stishovite at pressures exceeding 300 GPa - an unprecedented result. A derived stishovite structure from this study at pressures up to 336 GPa implies a skipping of three different second-order equilibrium phase transitions (CaCl_2 , $\alpha\text{-PbO}_2$ and pyrite-type structure) illustrating how complex structural changes are hindered during dynamic compression experiments.

Methods

Polycrystalline stishovite was synthesized using the large volume press housed at the PETRA III end station P61B at the German Electron-Synchrotron (DESY). Cylindrical pieces (3 mm in height, 2.5 mm in diameter) were cut from fused silica rods to fit precisely into a Pt-capsule. The Pt-capsule was placed at the center of a 18 mm edge length Cr₂O₃ doped MgO octahedral multi-anvil assembly. The octahedral assembly was heated to 1500 K for one hour after compressed to a maximum pressure of 12 GPa (see Supplementary Material). Samples were cut and polished to 35 (\pm 1) μ m and glued to 50 μ m thick black polyimide (kapton) tape. At LCLS, a Nd:glass optical laser (527 nm, 10 ns, quasi flat top pulse) in combination with 250- μ m diameter phase plates was used to launch a smooth and well defined laser pulse onto the targets. At SACLA, a ceramic YAG optical laser (532 nm, 5 ns, quasi flat top pulse) in combination with 300- μ m diameter phase plates was applied. Detailed information about the experimental platforms can be found in the references^{48,49}. Five different maximum drive laser energies were used for the experiments: 19.1 J and 22.1 J at SACLA, and 48.6 J, 50.6 J, 51 J at LCLS. Free surface velocities were recorded through the VISAR and shock velocities were calculated from velocimetry and diffraction data (see Supplementary Material). Two VISAR legs were employed to resolve fringe-jump ambiguity from the compressed sample velocity traces. The LCLS and SACLA FEL sources provided quasi-monochromatic (dE/E = 0.2–0.5%), coherent, 11.2 keV (LCLS) and 11 keV (SACLA) X-ray pulses of \sim 20 fs (LCLS) and \sim 7 fs (SACLA) duration. The XFEL beam at LCLS was focused to 50 \times 50 μ m² onto the target and centered to the focal spot of the drive laser. At SACLA, the XFEL beam was focused to 10 \times 30 μ m². The LCLS experiment was conducted in transmission geometry normal to the target whereas the SACLA experiment was conducted in reflection geometry with a grazing-incidence angle of 18° between sample surface and XFEL beam (Fig. 1). The XFEL probed the samples at shock breakout (\pm 0.5 ns), hence when the sample was completely compressed. Four Cornell-SLAC Pixel Array Detectors (CSPADs) at LCLS and a large flat panel detector (CMOS camera coupled with an X-ray scintillator) at SACLA recorded the resulting diffraction from the XFEL probe beam during shock compression. The diffraction images were azimuthally integrated and are shown as XRD pattern in Fig. 2.

Received: 17 March 2020; Accepted: 13 May 2020;

Published online: 23 June 2020

References

1. Stishov, S. & Popova, S. A new dense modification of silica. *Geochemistry* 923–926 – Trans. from Geokhimiya, 837–839 (1961).
2. Dmitriev, V., Toledano, P., Torgashev, V. & Salje, E. Theory of reconstructive phase transitions between SiO₂ polymorphs. *Phys. Rev. B* **58**, 11911 (1998).
3. Wicks, J. K. & Duffy, T. S. Crystal structures of minerals in the lower mantle. *Deep. earth: Phys. chemistry lower mantle core* **217**, 69–87 (2016).
4. Andrault, D., Fiquet, G., Guyot, F. & Hanfland, M. Pressure-induced Landau-type transition in stishovite. *Science* **282**, 720–724 (1998).
5. Andrault, D., Angel, R. J., Mosenfelder, J. L. & Le Bihan, T. Equation of state of stishovite to lower mantle pressures. *Am. Mineral.* **88**, 301–307 (2003).
6. Cohen, R. E. Calculation of elasticity and high pressure instabilities in corundum and stishovite with the potential induced breathing model. *Geophys. Res. Lett.* **14**, 37–40 (1987).
7. Tsuchida, Y. & Yagi, T. A new, post-stishovite high pressure polymorph of silica. *Nature* **340**, 217–220 (1989).
8. Kingma, K. J., Cohen, R. E., Hemley, R. J. & Mao, H.-K. Transformation of stishovite to a denser phase at lower-mantle pressures. *Nature* **374**, 243–245 (1995).
9. Hemley, R. *et al.* Strain/order parameter coupling in the ferroelastic transition in dense SiO₂. *Solid State Commun* **114**, 527–532 (2000).
10. Sun, N., Shi, W., Mao, Z., Zhou, C. & Prakapenka, V. B. High pressure-temperature study on the thermal equations of state of seifertite and CaCl₂-Type SiO₂. *J. Geophys. Res. Solid Earth* (2019).
11. Dera, P., Prewitt, C. T., Boctor, N. Z. & Hemley, R. J. Characterization of a high-pressure phase of silica from the martian meteorite shergotty. *Am. Mineral.* **87**, 1018–1023 (2002).
12. Murakami, M., Hirose, K., Ono, S. & Ohishi, Y. Stability of CaCl₂-type and a-PbO₂-type SiO₂ at high pressure and temperature determined by *in-situ* x-ray measurements. *Geophys. Res. Lett.* **30** (2003).
13. Dubrovinsky, L. *et al.* Pressure-induced transformations of cristobalite. *Chem. Phys. Lett.* **333**, 264–270 (2001).
14. Belonoshko, A. B., Dubrovinsky, L. S. & Dubrovinsky, N. A. A new high-pressure silica phase obtained by molecular dynamics. *Am. Mineral.* **81**, 785–788 (1996).
15. Grocholski, B., Shim, S.-H. & Prakapenka, V. Stability, metastability, and elastic properties of a dense silica polymorph, seifertite. *J. Geophys. Res. Solid Earth* **118**, 4745–4757 (2013).
16. Prakapenka, V., Shen, G., Dubrovinsky, L., Rivers, M. & Sutton, S. High pressure induced phase transformation of SiO₂ and GeO₂: difference and similarity. *J. Phys. Chem. Solids* **65**, 1537–1545 (2004).
17. Kuwayama, Y., Hirose, K., Sata, N. & Ohishi, Y. The Pyrite-Type High-Pressure Form of Silica. *Science* **309**, 923–925 (2005).
18. Akins, J. A. & Ahrens, T. J. Dynamic compression of SiO₂: A new interpretation. *Geophys. Res. Lett.* **29**, 31–1–31–4 (2002).
19. Lyzenga, G. A. & Ahrens, T. J. Shock temperatures of SiO₂ and their geophysical implications. *J. Geophys. Res.* **88**, 2431–2444 (1983).
20. Gleason, A. *et al.* Ultrafast visualization of crystallization and grain growth in shock-compressed SiO₂. *Nat. Commun.* **6**, 1–7 (2015).
21. Gleason, A. *et al.* Time-resolved diffraction of shock-released SiO₂ and diaplectic glass formation. *Nat. Commun.* **8**, 1–6 (2017).
22. Tracy, S. J., Turneare, S. J. & Duffy, T. S. *In situ* x-ray diffraction of shock-compressed fused silica. *Phys. Rev. Lett.* **120**, 135702 (2018).
23. Berryman, E. J., Winey, J. M., Gupta, Y. M. & Duffy, T. S. Sound velocities in shock-synthesized stishovite to 72 GPa. *Geophys. Res. Lett.* **46**, 13695–13703 (2019).
24. Luo, S.-N., Mosenfelder, J. L., Asimow, P. D. & Ahrens, T. J. Direct shock wave loading of Stishovite to 235 GPa: Implications for perovskite stability relative to an oxide assemblage at lower mantle conditions. *Geophys. Res. Lett.* **29**, 36–1–36–4 (2002).
25. Furnish, M. D., Shulenburg, L., Desjarlais, M. & Fei, Y. Recent research on stishovite: Hugoniot and partial release Z experiments and DFT EOS calculations (with nov. 17 2017 reanalysis). Tech. Rep., Sandia National Lab. (SNL-NM), Albuquerque, NM (United States) (2017).
26. Millot, M. *et al.* Shock compression of stishovite and melting of silica at planetary interior conditions. *Science* **347**, 418–420 (2015).
27. Wang, F., Tange, Y., Irifune, T. & Funakoshi, K.-I. P-V-T equation of state of stishovite up to mid-lower mantle conditions. *J. Geophys. Res. Solid Earth* **117** (2012).

28. Nishihara, Y., Nakayama, K., Takahashi, E., Iguchi, T. & Funakoshi, K.-I. P-V-T equation of state of stishovite to the mantle transition zone conditions. *Phys. Chem. Miner.* **31**, 660–670 (2005).
29. Panero, W. R., Benedetti, L. R. & Jeanloz, R. Equation of state of stishovite and interpretation of SiO₂ shock-compression data. *J. Geophys. Res. Solid Earth* **108**, ECV-5 (2003).
30. Ross, N. L., Shu, J. & Hazen, R. M. High-pressure crystal chemistry of stishovite. *Am. Mineral.* **75**, 739–747 (1990).
31. Angel, R. Eos-fit v6. 0. *Comput. program. Crystallogr. Lab. Dep. Geol. Sci. Virginia Tech, Blacksbg.* (2001).
32. Birch, F. Finite strain isotherm and velocities for single-crystal and polycrystalline NaCl at high pressures and 300 K. *J. Geophys. Res. Solid Earth* **83**, 1257–1268 (1978).
33. Watanabe, H. *et al.* Thermochemical properties of synthetic high-pressure compounds relevant to the Earth's mantle. *High-pressure Res. Geophys.* 441–464 (1982).
34. Buchen, J. *et al.* Equation of state of polycrystalline stishovite across the tetragonal-orthorhombic phase transition. *J. Geophys. Res. Solid Earth* **123**, 7347–7360 (2018).
35. Lee, C. & Gonze, X. SiO₂ stishovite under high pressure: Dielectric and dynamical properties and the ferroelastic phase transition. *Phys. Rev. B* **56**, 7321 (1997).
36. Černok, A. *et al.* Compressional pathways of α -cristobalite, structure of cristobalite XI, and towards the understanding of seifertite formation. *Nat. Commun.* **8**, 1–10 (2017).
37. Donadio, D., Martoňák, R., Raiteri, P. & Parrinello, M. Influence of temperature and anisotropic pressure on the phase transitions in α -cristobalite. *Phys. Rev. Lett.* **100**, 165502 (2008).
38. Kaercher, P. M. *et al.* Preferred orientation in experimentally deformed stishovite: implications for deformation mechanisms. *Phys. Chem. Miner.* **42**, 275–285 (2015).
39. Luo, S.-N., Ahrens, T. J. & Asimow, P. D. Polymorphism, superheating, and amorphization of silica upon shock wave loading and release. *J. Geophys. Res. Solid Earth* **108** (2003).
40. Simha, N. & Truskinovsky, L. Shear induced transformation toughening in ceramics. *Acta Met. Mater.* **42**, 3827–3836 (1994).
41. Smith, R. *et al.* Ultrafast dynamic compression technique to study the kinetics of phase transformations in bismuth. *Phys. Rev. Lett.* **101**, 065701 (2008).
42. Smith, R. *et al.* Time-dependence of the alpha to epsilon phase transformation in iron. *J. Appl. Phys.* **114**, 223507 (2013).
43. Rapp, L. *et al.* Experimental evidence of new tetragonal polymorphs of silicon formed through ultrafast laser-induced confined microexplosion. *Nat. Commun.* **6**, 1–10 (2015).
44. Gorman, M. *et al.* Femtosecond diffraction studies of solid and liquid phase changes in shock-compressed bismuth. *Sci. Rep.* **8**, 1–8 (2018).
45. Coleman, A. *et al.* Identification of phase transitions and metastability in dynamically compressed antimony using ultra-fast x-ray diffraction. *Phys. Rev. Lett.* **122**, 255704 (2019).
46. Pépin, C. M. *et al.* Kinetics and structural changes in dynamically compressed bismuth. *Phys. Rev. B* **100**, 060101 (2019).
47. Duffy, T., Madhusudhan, N. & Lee, K. Mineralogy of Super-Earth Planets. *Treatise on Geophys.* **2**, 149–178 (2015).
48. Nagler, B. *et al.* The matter in extreme conditions instrument at the Linac coherent light source. *J. Synchrotron Radiat.* **22**, 520–525 (2015).
49. Inubushi, Y. *et al.* Development of an experimental platform for combinative use of an XFEL and a high-power nanosecond laser. *Appl. Sci.* **10**(7), 2224 (2020).
50. Kerley, G. Equations of state for composite materials. *Rep. KPS99* **4** (1999).
51. Andraut, D. *et al.* Melting behavior of SiO₂ up to 120 GPa. *Phys. Chem. Miner.* **47**, 10 (2020).
52. Usui, Y. & Tsuchiya, T. Ab initio two-phase molecular dynamics on the melting curve of SiO₂. *J. Earth Sci.* **21**, 801–810 (2010).
53. Belonoshko, A. B. & Dubrovinsky, L. S. Molecular dynamics of stishovite melting. *Geochim. Cosmochim. Acta* **59**, 1883–1889 (1995).
54. Luo, S.-N., Čain, T., Strachan, A., Goddard, W. A. III. & Ahrens, T. J. Molecular dynamics modeling of stishovite. *Earth Planet. Sci. Lett.* **202**, 147–157 (2002).
55. Shen, G. & Lazor, P. Measurement of melting temperatures of some minerals under lower mantle pressures. *J. Geophys. Res. Solid Earth* **100**, 17699–17713 (1995).
56. Zhang, J., Liebermann, R. C., Gasparik, T., Herzberg, C. T. & Fei, Y. Melting and subsolidus relations of SiO₂ at 9–14 GPa. *J. Geophys. Res. Solid Earth* **98**, 19785–19793 (1993).

Acknowledgements

M.S., K.A., Th.Ts. and R.R. acknowledge support from the DFG (FOR 2440). A.G. acknowledges support from LANL Reines-LDRD. M.H. acknowledges support from the European Research Council (ERC) under the European Union's Horizon 2020 research and innovation program (grant agreement No. 670787 D PLANETDIVE). Use of the Linac Coherent Light Source (LCLS), SLAC National Accelerator Laboratory, is supported by the U.S. Department of Energy, Office of Science, Office of Basic Energy Sciences under Contract No. DE-AC02-76SF00515. The MEC instrument is supported by the U.S. Department of Energy, Office of Science, Office of Fusion Energy Sciences under Contract No. DE-AC02-76SF00515. This experiment was furthermore performed at BL3 of SACLA with the approval of the Japan Synchrotron Radiation Research Institute (proposal nos. 2019A8072). This work was supported by grants from MEXT Quantum Leap Flagship Program (MEXT Q-LEAP) grant no. JPMXS0118067246, Japan Society for the Promotion of Science (JSPS) KAKENHI (grant nos. 19K21866 & 16H02246), Genesis Research Institute, Inc. (Konpon-ken, Toyota). Financial support was also provided by the Federal Ministry of Education and Research, Germany (BMBF grant no.: 05K16WC2 & 05K13WC2). Parts of this research were carried out at the large volume press (LVP) beamline P61B at PETRAIII DESY Hamburg, a member of the Helmholtz Association (HGF). This study was also supported by National Science Foundation (EAR-1644614). The authors would like to thank the reviewers for their constructive comments.

Author contributions

Th.Ts., C.B., A.G., T.P., R.S., S.T., L.W., U.Z. and K.A. participated in the experiment at LCLS and contributed to the data analysis and interpretation. E.C., E.G. and B.N. each participated in the experiment as instrument scientists at MEC and contributed to data interpretation. Th.Ts., M.H., K.K., Ts.Tob., Y.U., N.O., T.P., L.W. and K.A. participated at the experiment at SACLA and contributed to the data analysis and interpretation. T.Y., Ta.Tog., K.M. and Y.I. participated in the experiment as instrument scientists at BL3:EH5 and contributed to data interpretation. K.A. and Th.Ts. were principal investigators. R.R. contributed in the data interpretation and DFT work. S.B. performed high-pressure synthesis of stishovite and R.F. supported and helped the synthesis at the large volume press at P61B of PETRAIII. M.S. took a lead role in the preparation, experiment, analysis of the data and writing of the paper. All authors reviewed the manuscript.

Competing interests

The authors declare no competing interests.

Additional information

Supplementary information is available for this paper at <https://doi.org/10.1038/s41598-020-66340-y>.

Correspondence and requests for materials should be addressed to M.O.S.

Reprints and permissions information is available at www.nature.com/reprints.

Publisher's note Springer Nature remains neutral with regard to jurisdictional claims in published maps and institutional affiliations.



Open Access This article is licensed under a Creative Commons Attribution 4.0 International License, which permits use, sharing, adaptation, distribution and reproduction in any medium or format, as long as you give appropriate credit to the original author(s) and the source, provide a link to the Creative Commons license, and indicate if changes were made. The images or other third party material in this article are included in the article's Creative Commons license, unless indicated otherwise in a credit line to the material. If material is not included in the article's Creative Commons license and your intended use is not permitted by statutory regulation or exceeds the permitted use, you will need to obtain permission directly from the copyright holder. To view a copy of this license, visit <http://creativecommons.org/licenses/by/4.0/>.

© The Author(s) 2020